Hindawi
Applied Bionics and Biomechanics
Volume 2023, Article ID 9930841, 16 pages
https://doi.org/10.1155/2023/9930841

Research Article

Numerical Study on Aerodynamic and Aeroacoustic Performances of Bioinspired Wings

Dichen Li and Chuang Wei

Aero Science Key Lab of High Reynolds Aerodynamic Force at High Speed, AVIC Aerodynamics Research Institute, Shenyang 110134, China

Correspondence should be addressed to Dichen Li; lidichen11@163.com

Received 14 April 2023; Revised 22 September 2023; Accepted 27 October 2023; Published 17 November 2023

Academic Editor: Marco Parente

Noise control has become one of the key issues to be considered in modern aeronautical machinery design. Many efforts have been devoted to noise reduction of airfoils and wings, including traditional flow control methods. In fact, some animals in wild nature exhibit superior aerodynamic and aeroacoustic performance, providing novel ideas for solving this engineering problem. In this research, bionic technology is used to obtain quiet and efficient wing. Inspired by the owl's wing, we propose two bionic configurations, one coupled with leading edge waves and trailing edge serrations. The Large Eddy Simulation and the Ffowcs-Williams and Hawkings equation is applied to simulate the aerodynamic and aeroacoustic characteristics of wings at low-Reynolds number flow. Numerical results demonstrate that the bioinspired wings have excellent aerodynamic performances and remarkable lower overall sound pressure level compared to NACA 0016 which has similar relative thickness. In addition, the unsmooth structure of leading edge waves and trailing edge serrations provide an additional 4.27 dB noise suppression effect, with little impact on aerodynamic characteristics at small angle of attack. The detailed analysis reveals that, due to the special owl-based profile, the flow around two bioinspired wings is mainly turbulent on the upper and lower surfaces, and no laminar separation bubble is detected at the trailing edge. Moreover, the unsmooth structure modifications successfully weaken the scale and scope of coherent vortex structures. These factors contribute to reducing the associated pressure fluctuation, thereby controlling the aeroacoustic noise of wing. Consequently, a coupled bionic wing is presented with the excellent aerodynamic and aeroacoustic characteristics. The conclusions are envisioned to be beneficial to the design of new generation low-noise aeronautical machinery.

1. Introduction

Presently, the rotary aeronautical machines at low-Reynolds number (Re) with an order of magnitude of 10^5, such as "flying car," civilian drones, micro aerial vehicles and turbomachinery, is getting an unprecedented high pace of development. Problems regarding to aerodynamic efficiency and noise control has gradually become urgent for academia and engineering circles. Noise pollution has already affected human's daily life, and caused great harm to human health. Stricter standards and regulations related to noise have been established by the governments all over the globe. Since airfoil/wing plays a key role in the performances of abovementioned machines, their aerodynamic and aeroacoustic characteristics is of utmost importance in the advanced design process. With regard to the noise reduction technologies, traditional active or passive approaches have proven to be efficient, but they are still limited by their inherent deficiencies like fabrication complexity, significant loss of the aerodynamic performance, low cost-effectiveness, and so on.

Owing to the natural selection over millions of years, genera of owls have evolved the ability to fly in silence, providing intriguing ideas for the design of low-noise machines. Through the investigation of the wings and feathers of owls, bionic structures have been utilized in aerodynamics and aeroacoustics study by considerable number of researchers. The pioneering work of Graham [1] found that the owl almost flies "silently" compared to the other birds due to its unique wing structures. Liu et al. [2] reconstructed the wings of four birds, i.e., seagull, merganser, teal, and owl by employing 3D scanning technology and extracted their airfoil profiles, which provides foundation for subsequent

experimental and numerical studies. Klän et al. [3, 4] experimentally studied the aerodynamics of owl wing in wind tunnel with the oil flow and particle image velocimetry (PIV). The wing model is constructed by 3D surface scan measurement. The separation bubble on suction surface is found to be the main feature and its size is reduced by applying the owl-specific velvet structures. Geyer et al. [5] used microphone array and six-component-balance in wind tunnel to investigate the aerodynamic and acoustic performance of prepared wings of the different bird species. The results show that the special wing and plumage adaptation are the reasons for silent flight of the owls rather than lower flight speed only. Ge et al. [6] built a bionic airfoil based on a long-eared owl wing, the study results suggest that the laminar separation bubble is formed on both upper and lower side of surface, and a distinct corresponding tonal noise characteristics at mid frequency is exhibited. Tian et al. [7] developed a bionic designing method of wind turbine blade which is inspired by long-eared owl's wing, such airfoil can provide superior lift coefficient and stall performance thus being beneficial to improving the efficiency of the turbine blade.

In addition to the aforementioned works, special bionic structures of trailing-edge serrations have been widely studied, which shows reduction of both broadband self-noise and instability tonal noise. Lilley [8] discovered that the leading edge comb-shaped feathers, trailing edge fringe shaped feathers, and fluff surface structures help owls reducing flight noise in the hearing frequency of their prey. Howe [9] is the first to apply the trailing edge serrations in noise reduction design of airfoil. The serrated structure directly facilitates reducing the noise. Chong et al. [10, 11] confirmed the tonal noise reduction effect of serrated trailing edge at low-Reynolds number. The experiments support the theory of aeroacoustic feedback loop which involves the Tollmien–Schlichting (T–S) waves and radiated acoustic wave from trailing edge. By influencing the connection of T–S wave and laminar separation bubble, the trailing edge serration can effectively achieve the suppression of airfoil instability self-noise. Gruber et al. [12] conducted an experiment involving over 30 different geometries of serrated trailing edges on a NACA 6512 airfoil, in which serration parameters are comprehensively investigated regarding to noise reduction. Results suggest that sharper serrations have greater noise control effect over a wide frequency range, but increased noise at higher frequencies can also have adverse effects. Moreau and Doolan [13] experimentally analyzed the flow and noise of two trailing edge serrations on a flat-plate model at a low-Reynolds number. It shows that the wider serrations reduce the overall sound pressure level (SPL) by up to 11 dB but the narrower serrations produce tonal noise and increase the overall noise level by up to 4 dB. Based on the integration of the Central Composite Design and the Response Surface Method, Liu et al. [14] carried out an investigation about optimizing the NACA 0018 airfoil's serrated trailing edge. The optimized configuration shows a 2 dB overall SPL reduction due to the suppression of laminar separation bubble.

The concept of bionic leading edge noise reduction of airfoil originates from human's understanding of the owl wing structure. However, the sharp serrated structures of an owl's wing bring great manufacturing difficulties, thus limiting the engineering applications. Therefore, in view of the airfoil leading edge noise reduction, focus has gradually shifted to the humpback whale flipper leading-edge rounded protuberances (also called tubercles). In 1995, Fish and Battle [15] published the groundbreaking study, in which the morphological analysis and fluid mechanical performance of protuberances in the humpback whale flipper leading-edge is investigated. Since then, many scholars have studied the fluid dynamics of this structure, and found that such structures can significantly improve the wing stall performances due to reduction of flow separation [16, 17]. Hansen et al. [18] are the first to study the tonal noise control effect of NACA 0021 airfoil with sinusoidal leading edge tubercles. The significant reduction of tonal noise together with the overall broadband noise surrounding its spectrum peak is witnessed. Chong et al. [19] carried out a systematic wind tunnel experiment of wavy leading edge airfoils with the different wave lengths and amplitudes, and results show that bigger amplitude and smaller wavelength have better noise suppression effect. Ito [20] performed wind tunnel experiments with wing model attached with Jigsaw serrations, aiming to imitate the leading edge serrated feather on an owl wing. The author came to a conclusion that the aerodynamic and aeroacoustic characteristics of fine serrations have a strong Reynolds number effect, improvement of lift coefficient and control of flow separation appears notably only at low-Reynolds number and larger angle of attack (AoA). The numerical study of Haeri et al. [21] shows that the noise level of flat-plate airfoil decreased linearly with the amplitude of leading edge waves, and the noise reduction mechanism is related with the interference effects of different wave regions. Narayanan et al. [22] experimentally investigated the effect of leading edge serrations as a means of reducing the broadband noise. It is observed in the parameter characteristics analysis that the sound power reduction level is sensitive to the serration amplitude but much less sensitive to the wavelength. And the results also reveal that the noise reductions are not significant at low frequencies, but is significant in the intermediate frequency range (500–8,000 Hz). Clair et al. [23] applied the concept of sinusoidal leading edge serration to reduce the turbofan broadband noise. The experiment and numerical simulations of isolated NACA airfoils show that significant noise reductions on a wide frequency range for all studied flow speeds, while maintaining the aerodynamic performances. More recently, Paruchuri et al. [24] proposed innovative leading-edge geometries that can offer considerable noise reductions, including double-wavelength serration, chopped-peak airfoil, and slitted-root serration. And the analysis show that their mechanism is associated with either being control of source or control of radiation. Wang et al. [25] analyzed different geometries of leading edge waves on NACA 0012 airfoil, including sinusoidal, serrated, and iron-shaped. The results show that the airfoil with iron-shaped leading-edge waves presents with highest noise reduction of 14.3 dB, and the change of vorticity induced by biomimetic structures is the suggested cause. Bruce Ralphin Rose et al.'s [26–29]

group conducted comprehensive reviews toward the biomimetic flow control techniques in the aerodynamic applications. Moreover, the straight and sweptback wings with the humpback whale leading edge tubercles are studied numerically and experimentally, which show enhanced aerodynamic performances.

In all, different influences of aerodynamic and aeroacoustic characteristics have been exhibited by the special bioinspired configurations, such as the avian airfoil profile, leading edge/trailing edge serrations, and surface ridges. However, the mechanisms regarding to such significant phenomena like noise generation and dissipation has not reached a consensus by scholars, inconsistent conclusions even appear in the experimental and numerical analysis, and different explanatory theories still need further investigations. Furthermore, the majority of the studies only consider one aspect of biostructures of bionic profile, leading edge and trailing edge structures, which rarely couple these factors together. Therefore, the benefits and underlying mechanism of the multifactor-coupled bionic wing has not been fully understand, and associated design innovations are greatly restricted. In present study, we propose a "bionic wing" which is reconstructed by the reverse engineering of barn owl wing's cross-section, and another "coupled bionic wing" which is further coupled with leading-edge waves and trailing-edge serrations. The numerical approach of the Large Eddy Simulation (LES) method coupled with Ffowcs-Williams and Hawkings (FW–H) acoustic equation is employed, the subgrid-scale model we used is Wall-Adapting Local Eddy-Viscosity (WALE) model. The influence of the aerodynamic and aeroacoustic characteristics of two bioinspired wings is analyzed. The conclusions will help to understand the noise reduction mechanism of bionic technology and providing reference for the design and performance evaluations of aeronautical machines.

2. Geometry Modeling

In order to study the aerodynamic and aeroacoustic characteristics of the owl-based wing, establishment of an airfoil model is the first step. By using 3D laser scanner, Liu et al. [2] first carried out the reconstruction of a bionic airfoil based on natural avian wings. In accordance to Liu's method, Klän et al. [3] reconstructed a novel owl-based airfoil. The obtained airfoil model is more natural to real owl with parameter modifications. The present study utilizes the above method to reconstruct a barn owl-based airfoil, for the purpose of comparing with conclusion in the previous literature that mainly study flat-plates or NACA series airfoil.

The distribution of the upper and lower surfaces profiles of an owl-based airfoil profile can be obtained as follows:

$$z_{\text{upper}} = z_c + z_t, \tag{1}$$

$$z_{\text{lower}} = z_c - z_t. \tag{2}$$

The camber line is described by a Birnbaum–Glauert function:

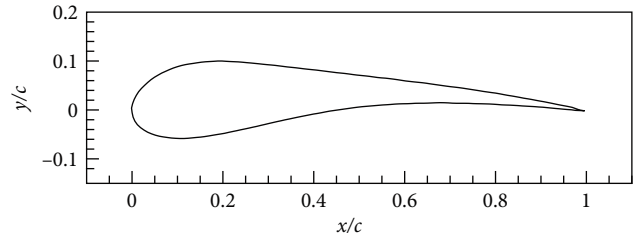

Figure 1: Bionic owl-based airfoil profile.

$$\frac{z_c}{c} = \frac{z_{c(\max)}}{c}\eta(1-\eta)\sum_{n=1}^{3} S_n(2\eta-1)^{n-1}. \tag{3}$$

And the thickness distribution by:

$$\frac{z_t}{c} = \frac{z_{t(\max)}}{c}\sum_{n=1}^{4} A_n\left(\eta^{n+1} - \sqrt{\eta}\right), \tag{4}$$

where x is the chordwise position, c is the local chord length, and $\eta = x/c$ is the normalized chordwise position. The quantities S_n and A_n are the coefficients of polynomials, their value is obtained by least-squares method. In present work, the coefficients S_n along the span for the camber line are: $S_1 = 0.1503$, $S_2 = -0.002841$, and $S_3 = 0.001188$, and the coefficients A_n for the thickness distribution are $A_1 = -1.912$, $A_2 = 4.005$, $A_3 = -3.451$, and $A_4 = 1.091$. The maximum camber line coordinate and the maximum thickness coordinate are denoted as $z_{c(\max)}$ and $z_{t(\max)}$, expressed by:

$$\frac{z_{c(\max)}}{c} = \frac{0.18}{1 + 7.31\xi^{2.77}}, \tag{5}$$

$$\frac{z_{t(\max)}}{c} = \frac{0.1}{1 + 14.86\xi^{3.52}}, \tag{6}$$

where ξ is the spanwise location.

Previous work of long-eared owl [30] suggests that a 40% spanwise location of the owl wing has better performance of aerodynamics and noise reduction. Consequently, in present study of barn owl, the spanwise location $\xi = 0.4$ is also selected. By utilizing the above-mentioned equations, the airfoil in the selected position of the owl wing can be extracted. The resulting bionic airfoil profile is demonstrated in Figure 1. The owl-based airfoil has a relatively thick leading edge and sharp trailing edge. The basic geometric parameters of the bionic airfoil are displayed in Table 1. The proposed "bionic wing" is constructed by a spanwise extension of this profile.

In addition to special bionic airfoil, the unsmooth structures on the owl wing and humpback whale flipper also play a significant role in the noise and flow control. These factors are integrated into the construction of the coupled bionic wing. To be specific, the tubercles on the leading-edge of humpback whale flipper can be treated like wavy structure, which in the form of sinusoidal profiles with wavelength λ and amplitude A. The serration on the owl wing's trailing

Table 1: The basic geometric parameters of the bionic airfoil.

Variable	Value
Chord length	c
Maximum thickness	15.52%c
Position of maximum thickness	0.16c
Maximum camber	3.77%c
Position of maximum camber	0.51c

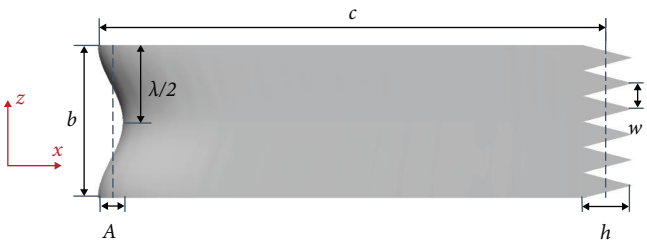

Figure 2: Sketch of coupled bionic wing.

Table 2: Geometrical parameters of bionic structures on wing.

Variable	Value
Wavelength, λ	0.3c
Amplitude, A	0.05c
Serration height, h	0.1c
Serration width, w	0.05c

edge can be regarded as Jigsaw serrations, which is characterized by the its height h and width w. Figure 2 shows a sketch of these unsmooth structures on the wing. The number of unsmooth elements present along the span depends on the structure parameters. Based on the morphology found on the leading edge of humpback whales' flippers, the amplitude and wavelength of the tubercles range from 2.5%–12% and 25%–50% of the local chord along the span, respectively [31]. And the suggested height and width of owl wing trailing edge serrations are 5%–15% and 5%–10% of the local chord along the span, respectively [32, 33]. In this study, the design parameters of the leading edge wave and trailing edge serration of the coupled bionic wing are selected from above ranges after several manual trials based on our experiences, as shown in Table 2, single leading edge wave and six trailing edge serration periods are arranged. It should be noted that they may not be the optimal parameters. Due to the occurrence of certain complex nonlinear variation pattern in our rough trials, and lack of universal law on the effect of parameters in previous literature, in which some conclusions may even contradict each other, a comprehensive parametric study and fully automated optimization design is needed for further study.

As for both wings, the chord length c and span width b are 200 and 60 mm, respectively ($b = 0.3c$). Figure 3 shows the constructed "bionic wing" and "coupled bionic wing". The average leading edge and trailing edge baselines of the waves and serrations coincide with the smooth wing so that the overall projected area of the wing on the horizontal plane basically remains the same.

3. Numerical Methodology

In this study, the unsteady flow is solved by LES to obtain the aerodynamic characteristics. SPL around the wing is then calculated from the fluctuating surface pressure based on the FW–H equation. This method has been proved to be accurate and efficient to predict the aerodynamic and aeroacoustic characteristics in various cases [34–36].

3.1. Basic Equations of LES. Since the velocity involved in this work is rather low (Ma = 0.06), the flow can be regarded as incompressible. The incompressible governing equations of LES method are derived by a filtering operation on the incompressible Navier–Stokes (N–S) equations. The filtered governing equations are as follows:

$$\rho \frac{\partial \overline{u}_i}{\partial x_i} = 0, \tag{7}$$

$$\rho \frac{\partial \overline{u}_i}{\partial t} + \rho \frac{\partial \overline{u}_i \overline{u}_j}{\partial x_j} = -\frac{\partial \overline{p}}{\partial x_i} + \frac{\partial}{\partial x_i}\left(\mu \frac{\partial \overline{u}_i}{\partial x_j} - \tau_{ij}^r\right), \tag{8}$$

where the overbar denotes the filtering operation, and the subgrid-scale stresses (SGS) tensor τ_{ij}^r, which is the modeling target of LES method, is given by the following expression:

$$\tau_{ij}^r = \rho\overline{u_i u_j} - \rho\overline{u}_i\overline{u}_j. \tag{9}$$

The wall adapting-local eddy-viscosity (WALE) [37] model is used in the current article to solve the filtered small-scale eddies. The WALE model guarantees that the turbulent viscosity goes to zero naturally at walls, so no forcing constant or damping function is needed. Since its publication, the model works well for simulating the transient flows filed in complex geometry by many researchers [38]. The SGS stress is linked to the filtered strain-rate tensor $\overline{S}_{ij}$:

$$\tau_{ij}^r = -2\mu_t \overline{S}_{ij} + \frac{1}{3}\delta_{ij}\tau_{kk}, \tag{10}$$

where μ_t is the eddy subgrid-scale turbulent viscosity. Definition of the turbulent viscosity is given as follows by WALE model:

$$\mu_t = \rho {L_s}^2 \frac{\left(S_{ij}^d S_{ij}^d\right)^{3/2}}{\left(\overline{S}_{ij}\overline{S}_{ij}\right)^{5/2} + \left(S_{ij}^d S_{ij}^d\right)^{5/4}}, \tag{11}$$

where L_s and S_{ij}^d are defined as follows:

$$L_s = \min\left(\kappa d, C_w V^{1/3}\right), \tag{12}$$

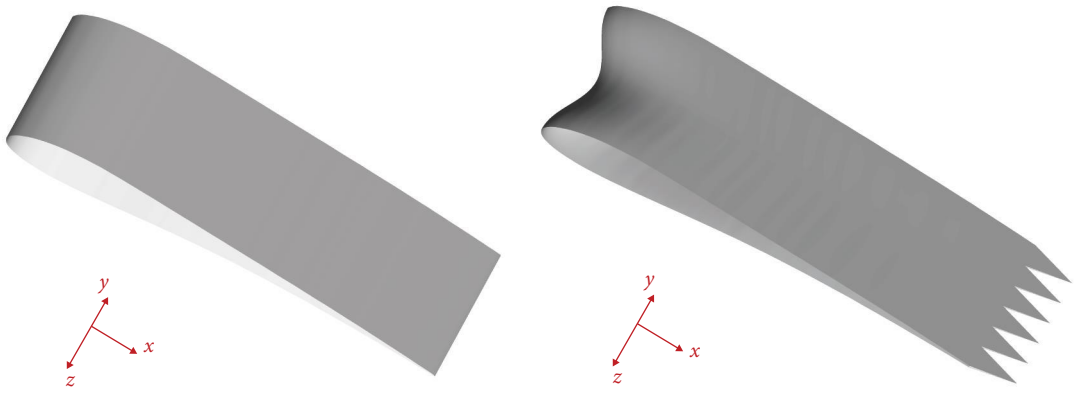

(a) (b)

FIGURE 3: Geometrical models of two types of bioinspired wings. (a) Bionic wing. (b) Coupled bionic wing.

$$S_{ij}^{d} = \frac{1}{2}\left(\overline{g}_{ij}^{2} + \overline{g}_{ji}^{2}\right) - \frac{1}{3}\delta ij\overline{g}_{kk}^{2}, \overline{g}_{ij}^{2} = \frac{\partial \overline{u}_i}{\partial x_j}. \tag{13}$$

Here, κ is a von Kármán constant, d is the distance to the closest wall. C_w is the Smagorinsky constant, and a default value of 0.325 is assigned in the WALE subgrid model.

3.2. FW–H Equation. In this paper, the FW–H equation [39, 40] is used for computing sound. The FW–H equation is essentially an inhomogeneous wave equation that can be derived by manipulating the continuity equation and the N–S equations, given by the following expression:

$$\begin{aligned} \frac{1}{a_0^2}\frac{\partial^2 p'}{\partial t^2} - \nabla^2 p' &= \frac{\partial^2}{\partial x_i \partial x_j}\left\{T_{ij}H(f)\right\} \\ &- \frac{\partial}{\partial x_i}\left\{\left[P_{ij}n_j + \rho u_i(u_n - v_n)\right]\delta(f)\right\}, \\ &+ \frac{\partial}{\partial x_i}\left\{\left[\rho_0 v_n + \rho(u_n - v_n)\right]\delta(f)\right\} \end{aligned} \tag{14}$$

where u_i is the fluid velocity component in the x_i direction, u_n is the fluid velocity component normal to the surface, v_i is the surface velocity components in the x_i direction, v_n is the surface velocity component normal to the surface, and $\delta(f)$ and $H(f)$ are Dirac delta function and Heaviside function, respectively. p' is the unsteady sound pressure fluctuation at the far field, a_0 is the sound propagation speed, P_{ij} is the compressive stress tensor, T_{ij} is the Lighthill stress tensor, defined as follows:

$$T_{ij} = \rho u_i u_j + P_{ij} - {a_0}^2(\rho - \rho_0)\delta_{ij}. \tag{15}$$

In the right-hand side of Equation (14), the first term represents the quadrupole source generated by a volumetric source. The second and third terms indicate that dipole and monopole sources have surface source characteristics, which are caused by the action of fluid on the wing surface and the change in fluid volume, respectively. In this study, since the flow is considered incompressible (Ma < 0.3), the quadrupole source can be ignored because the ratio of the intensity of quadrupole source to a dipole source is proportional to the square of the Mach number. Besides, the studied wings are considered as rigid bodies, the fluctuation of volume is too low to influence the airflow effectively, thus the monopole source is also ignored. Therefore, it is suggested that the dipole source is predominant and make a major contribution to the noise generation in this work.

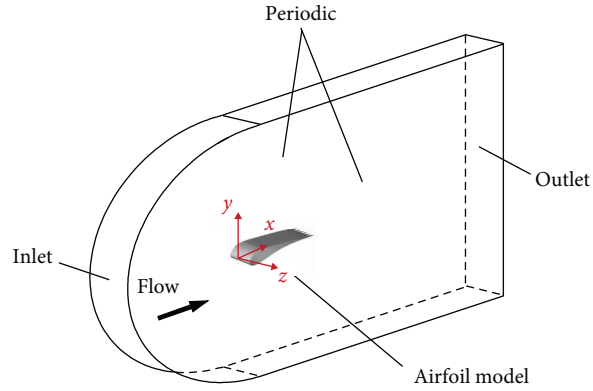

FIGURE 4: Overview of computational domain and boundary conditions.

3.3. Computational Condition. Treatment of calculation domain is critical to a numerical simulation, because boundaries and the associated boundary conditions define the problem to be solved. Figure 4 illustrates the computational domain and the boundary conditions. The calculation domain is established as a combination of a semicylinder and cuboid model. The calculation domain should be large enough to avoid the reflection interference of boundaries. The origin of coordinates is defined at the leading edge of the wings. The distance from the bioinspired wing to the upstream and downstream is 10c and 20c, respectively. The width of spanwise direction is equal to the wing span. The front surface as well as the top and bottom are set as the velocity-inlet boundary condition. And the incoming freestream velocity is 20 m/s according to the normal flight

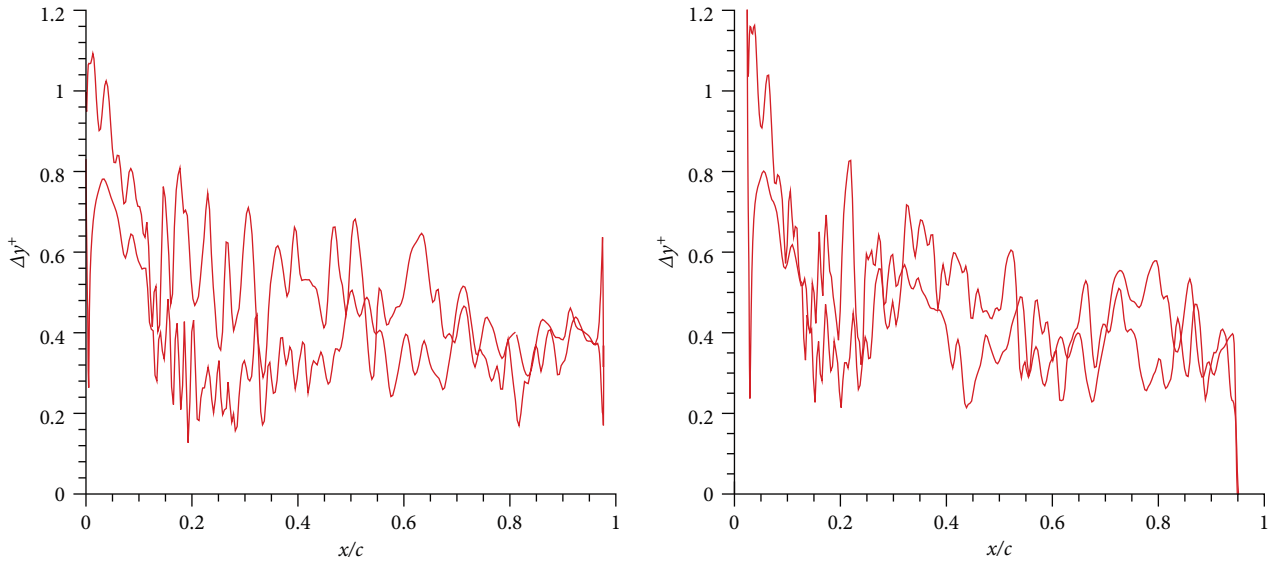

FIGURE 5: The Δy^+ distribution of the bioinspired wing surface at midspan. (a) Bionic. (b) Coupled bionic.

velocity of barn owl, which can be considered as turbulent incompressible flow. The Reynolds number based on the bionic airfoil chord is approximately 2.74×10^5, which belongs to the typical low-Reynolds number flow regime in the aeronautical applications. The rear surface is set as the pressure-outlet boundary condition with 101,325 Pa as in ambient atmosphere. The two side surfaces in are set as translational periodic boundary conditions, as it has been widely adopted in the previous studies and proven to be an appropriate choice [41]. The no-slip wall boundary condition is applied to the wing surfaces.

In the current study, the finite-volume method (FVM) is used to numerically simulate unsteady turbulence based on incompressible LES. The pressure–velocity coupling scheme is based on the SIMPLEC algorithm. The Green–Gauss node-based gradient method is used to solve the gradients of variables. The bounded central differencing and bounded second-order implicit scheme are adopted for discretizing the momentum and transient formulation to reduce numerical dissipation. To capture subtle turbulent flow phenomena, the unsteady physical time step is set to $\Delta t = 2 \times 10^{-5}$ s to yield a global Courant number less than 1, which resulting in the sampling frequency upper limit 25 kHz of acoustic spectra. The acoustic signals are calculated for a total physical time 0.1 s.

3.4. Grid Independency and Verification. In view of the geometrical complexity of the unsmooth structures of the bioinspired wings, it is a better choice to employ the unstructured grid for its superior adaptability to complex configurations. In fact, although structured grid is used in many relevant works by body-fitted or immerse boundary techniques, the unstructured grid has already been adopted in LES and its reliability has been well-verified [38, 42, 43]. For LES model, certain resolution requirements of grids in the near-wall region need to be satisfied for solving the near-wall gradients [44]. Given that the friction velocity $u_\tau = \sqrt{\tau_\omega/\rho}$, the distance from the wall measured in viscous length can be evaluated as $\Delta y^+ = u_\tau y/\nu$. In a similar manner the streamwise Δx^+ and spanwise Δz^+ cell sizes can be obtained. Specifically, in present study, to well resolve the boundary layers, the grid spacing for the streamwise and spanwise directions meet the range of $\Delta x^+ \leq 50$ and $\Delta z^+ \leq 30$, respectively. And the distances from the wall of the first control volume mainly satisfy $\Delta y^+ < 1$, as shown in Figure 5.

To determine the appropriate grid number, the grid independence test needs to be conducted. In this study, three different grids, labeled as *Coarse*, *Medium*, and *Fine*, with different density levels are analyzed based on the bionic wing at AoA = 5°. For the coupled bionic wing, the surface grids near the leading/trailing edge and their adjacent volume region are refined to characterize the unsmooth structures, the rest node distributions remain unchanged, and thus the grid keeps a similar density level though a little denser than that of the bionic wing.

The variation of drag coefficient (C_D) with time is used as a monitor for calculation convergence. The flow field data of 0.3–0.5 s, at which calculation is well-converged, are adopted for time-averaged processing and further analysis. Figure 6 shows the time-averaged drag coefficient of three grids. It can be seen that the drag values calculated by three grids show converging trend as it becomes denser. For grid *Medium* and *Fine*, there is only less than 0.6% difference observed between their calculated results. Therefore, considering the balance between numerical accuracy and computing time, the *Medium* level grid density should be sufficient enough for the currently concerned flow, and this density level will be used for grid generations hereafter. Figure 7 shows the computational grids of two bioinspired wings.

To further validate the effectiveness and accuracy of the numerical method in this paper, both the pressure coefficient distributions C_p and skin friction coefficient distribution C_f

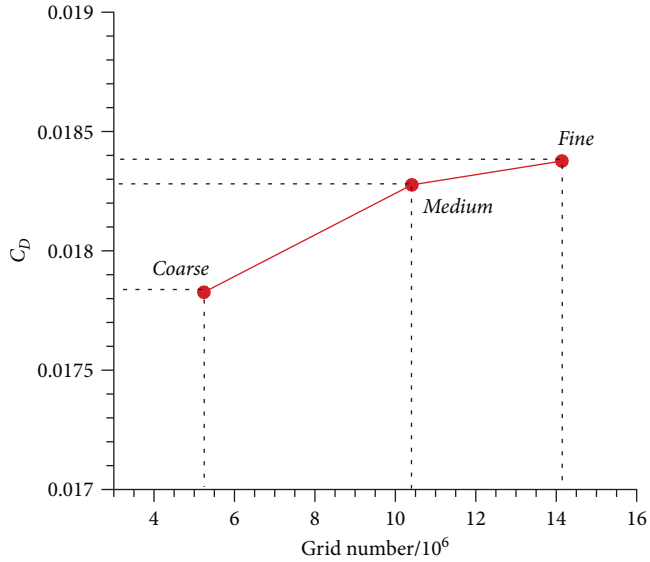

Figure 6: Time-averaged drag coefficient.

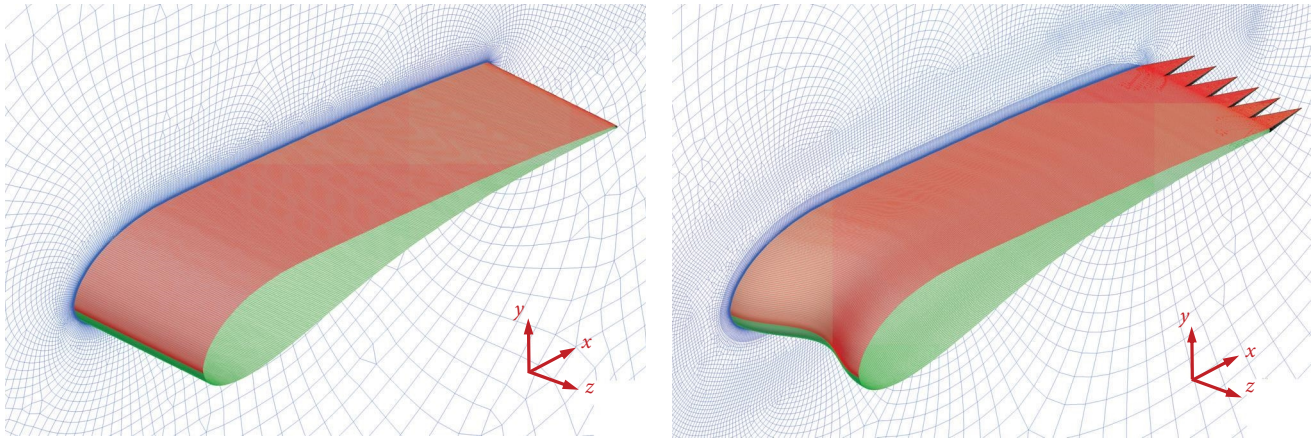

(a) (b)

Figure 7: Computational grids of two bioinspired wings. (a) Bionic wing. (b) Coupled bionic wing.

based on the NACA 0012 wing at Reynolds numbers $Re = 5.47 \times 10^4$, AoA = 5°, together with the results of Lehmkuhl et al. [38], are utilized for illustration and comparison in Figure 8. It shows that the numerical results consist well with the direct numerical simulation (DNS) results in the reference. The flow separation, transition, and reattachment (i.e., laminar separation bubble) on the airfoil surface has been well-simulated with considerable accuracy. For the calculation of far-field aeroacoustic characteristics, many verification works [45, 46] based on LES + FWH method have been carried out for flow past cylinder case. Here, the present result of airfoil self-noise is compared with the classic experimental measurement of Brooks et al. [47] and simulation of Jafari et al. [48]. The flow parameters and sound receiver position are set according to those literatures. In Figure 9, the SPL spectra for the NACA 0012 airfoil at Reynolds number $Re = 2 \times 10^5$, AoA = 0°, at location 1.25 m perpendicular to the trailing edge are plotted via fast Fourier transformation (FFT). The comparison of both the narrow-band and 1/3 octave-band SPL results show that the present numerical results are in good agreement with those literature data for the different frequencies, except for the 1,000-Hz frequency range around, where the sound level is slightly lower. This is possibly due to the difference in airfoil trailing-edge bluntness, as airfoil model used in our calculation has bluntness of about 0.003c, which is much bigger than the sharp trailing edge in experiment. The obtained numerical results truly predict the experimental data growth and descend. Thus, the LES + FW–H method is well-verified and used for the calculations hereafter.

4. Result and Discussion

4.1. Aerodynamic Performance. The aerodynamic characteristics of lift coefficient (C_L) and drag coefficient (C_D) based on the characteristic length and area are determined with the following expressions:

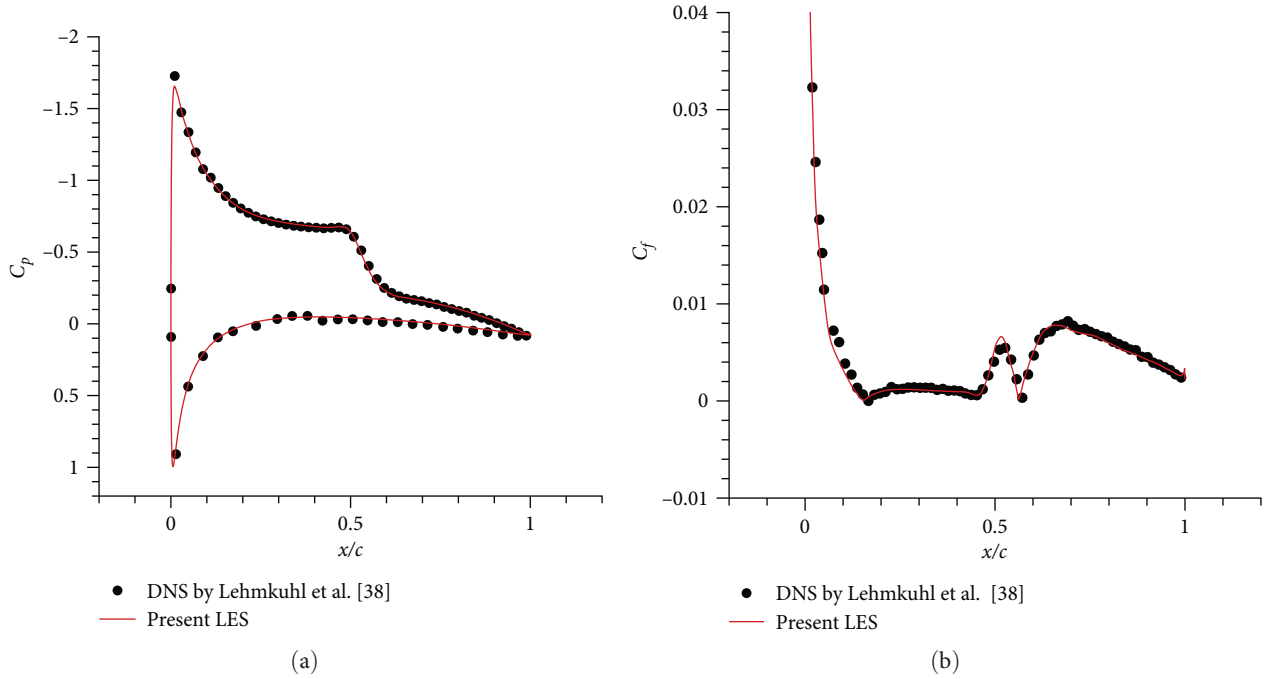

Figure 8: Aerodynamic comparison between LES and DNS of NACA 0012 wing. (a) Pressure coefficient. (b) Skin friction coefficient.

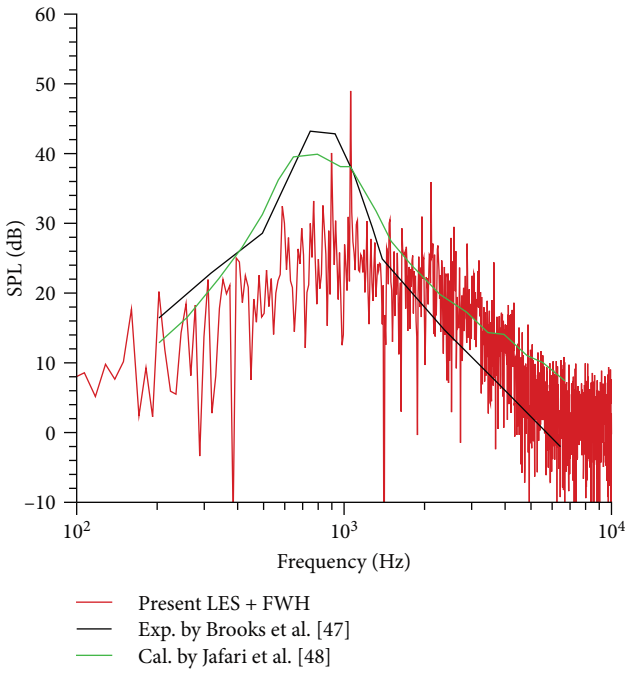

Figure 9: Aeroacoustic spectra comparison of NACA 0012 wing.

$$C_L = \frac{L}{0.5\rho U_0^2 S}, \tag{16}$$

$$C_D = \frac{D}{0.5\rho U_0^2 S}, \tag{17}$$

where L and D denote the lift force and drag force, respectively. S is the characteristic area, here it refers to the projected area of the wing on the horizontal plane. Figure 10 shows the comparison of aerodynamic characteristics, including the lift coefficient and drag coefficient, for the studied wings. The performance of conventional NACA 0016 airfoil is also shown here, with a relative thickness of 16% similar to that of two bioinspired wings, it serves as a good reference for comparison, since the maximum relative thickness has a significant influence on the aerodynamic and aeroacoustic characteristics of airfoil [49, 50]. It is quite clear that two bioinspired wings present the same tendency. The lift shows no presence of stall below AoA = 15°, and basically remains unchanged with unsmooth modifications. A value of $C_L \approx 0.99$ at AoA = 5° is identified for both wings, for instance, which is higher than that of symmetrical NACA 0016 ($C_L = 0.484$) and classical low-Reynolds airfoil E387 ($C_L = 0.9514$, calculated by *XFoil*). The drags of two bioinspired wings are, however, both higher than NACA 0016 at AoA = 5° with nearly 39.4% enhancement. Discrepancies of two bioinspired wings progressively become evident at high AoAs, the coupled bionic wing is presented with larger drag at AoA = 15°, whereas satisfactory agreement shows at small AoAs with only 5.0% drag difference as at AoA = 5°. It can be concluded that the special owl-based wing has excellent aerodynamic performances at low-Reynolds number condition. And the leading edge waves and trailing edge serrations have little influence on aerodynamic characteristics in small working angle before stall. This might give the animal superior capability during their glide and predation.

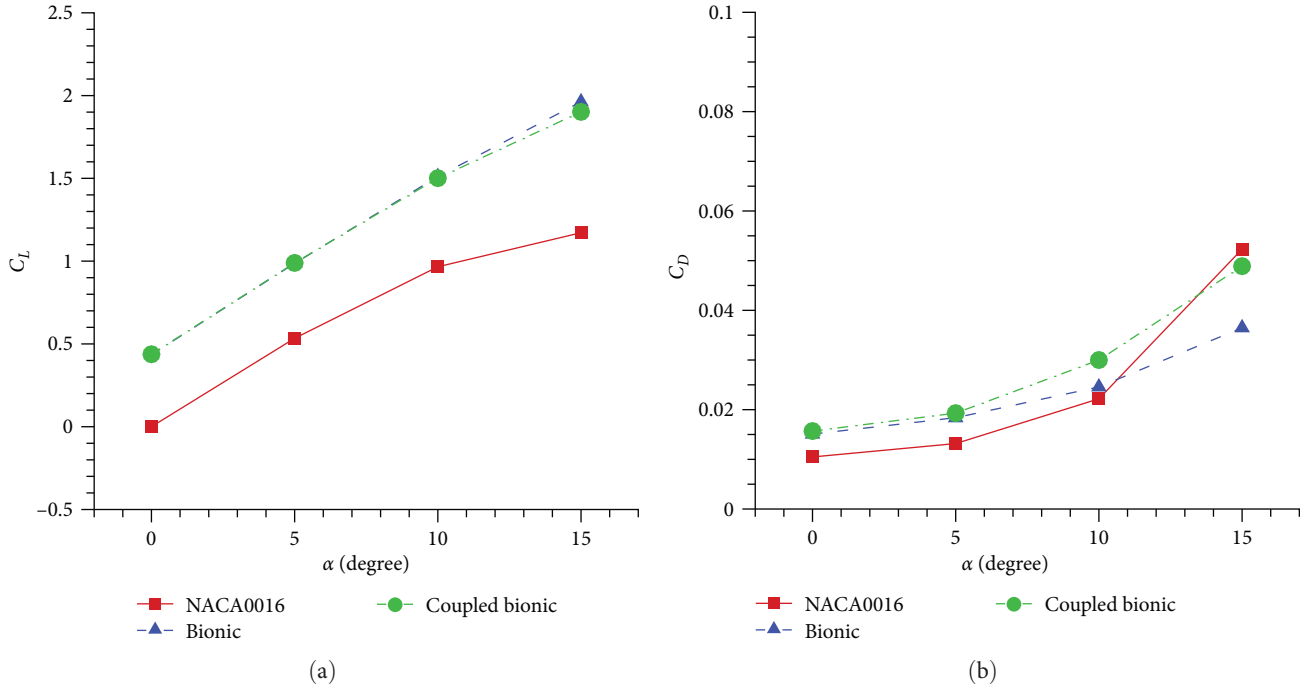

Figure 10: Aerodynamic characteristics of wings. (a) Lift coefficient. (b) Drag coefficient.

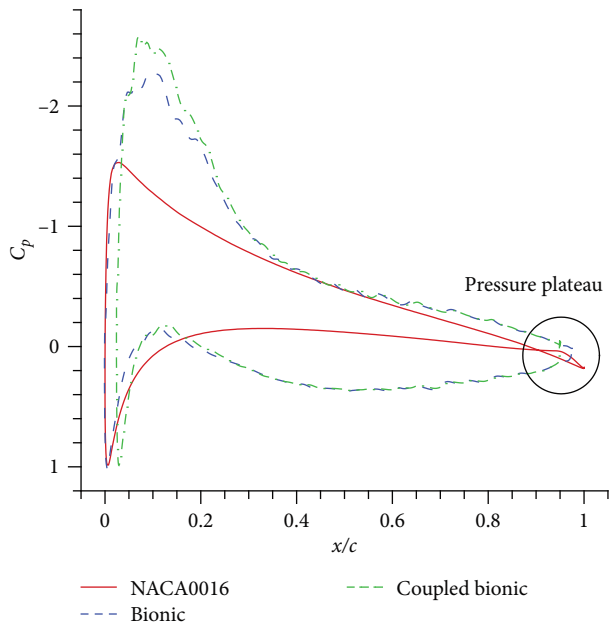

Figure 11: The mean pressure coefficient distributions of NACA 0016, bionic wing and coupled bionic wing.

The time-averaged pressure coefficient distribution at midspan is further presented in Figure 11. To accord with the acoustic analysis, AoA = 5° is selected here. It is obvious that for two bioinspired wings, the pressure distribution is similar. Strong adverse pressure gradients exist on both the upper and lower surface, which is mainly caused by the special airfoil profile. The differences appear at the leading edge and trailing edge, where unsmooth structures slightly alter the pressure distribution. Yet the enclosed area of *Cp* curve almost remains unchanged, thus leading to very little difference (≈0.26%) of lift coefficient. However, the symmetric NACA 0016 shows a tremendously decreased area, therefore less lift coefficient is achieved. It is also interesting to notice that the NACA 0016 lower surface exhibits a smooth positive pressure gradient. And at the trailing edge region, a small "pressure plateau" occurs, which indicating a classical low-Reynolds number laminar separation bubble is formed here. Similar phenomenon is also witnessed in NACA 0012 and NACA 0018, and is considered as a necessity for the generation of tonal noise [11, 51].

4.2. Flow Field Structures. As shown in Figure 12, the turbulence contour with streamlines of NACA 0016, bionic wing and coupled bionic wing at AoA = 5°of midspan are depicted, in order to visually analyze the time-averaged aerodynamic characteristics and flow filed structures. The turbulence intensity is generally defined as the ratio of turbulent fluctuating velocity to averaged velocity. It is a sensitive index to differentiate between laminar and turbulent flow. The turbulence intensity distribution of NACA 0016 is different from that of two bioinspired wings. It can be seen that no high value of turbulence exhibited around the lower surface of NACA 0016, which indicates that flow is laminar under smooth positive pressure gradient. Except for the trailing edge region, as clearly demonstrated by zoom-in streamlines, where laminar separation bubble brings about the two-dimensional spanwise vortices shedding off and mixing with upper fully developed turbulence. Contrarily, no separation detected for two bioinspired wings, as manifested by the attached streamlines. The high-turbulence intensity occurs in a similar pattern at the front of both the upper

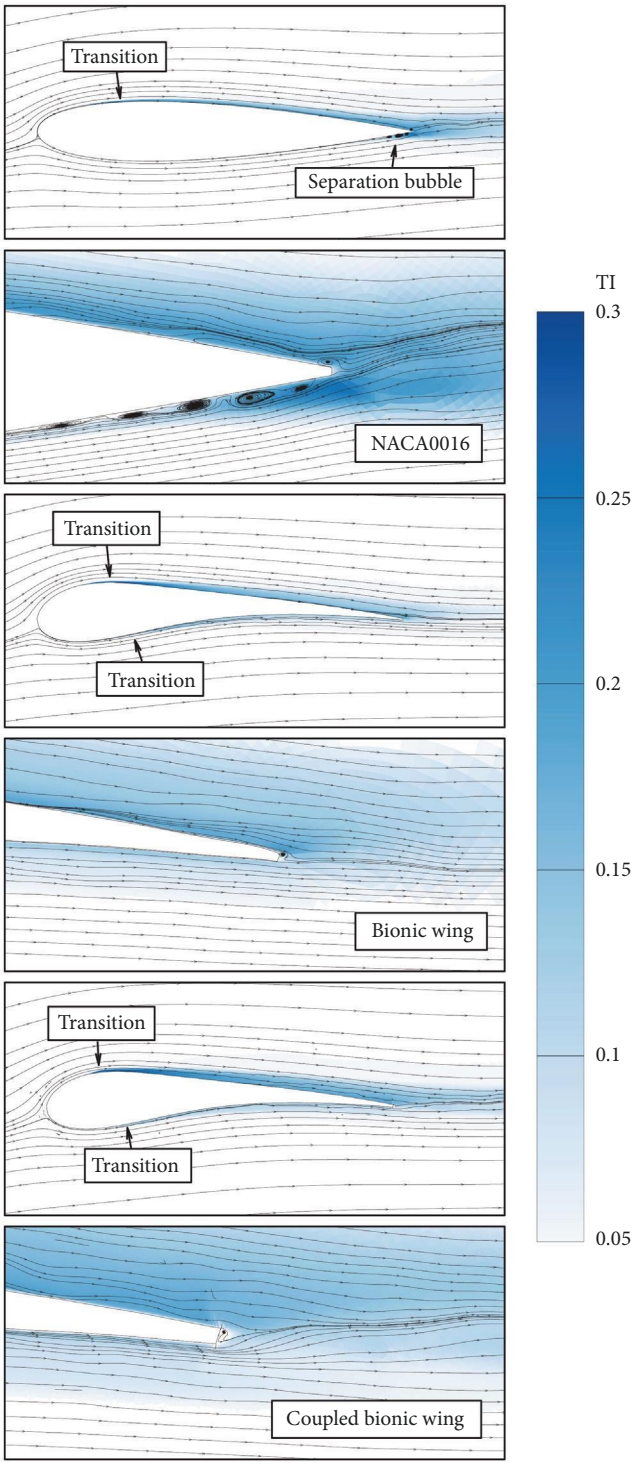

Figure 12: The turbulence intensity contour with streamline.

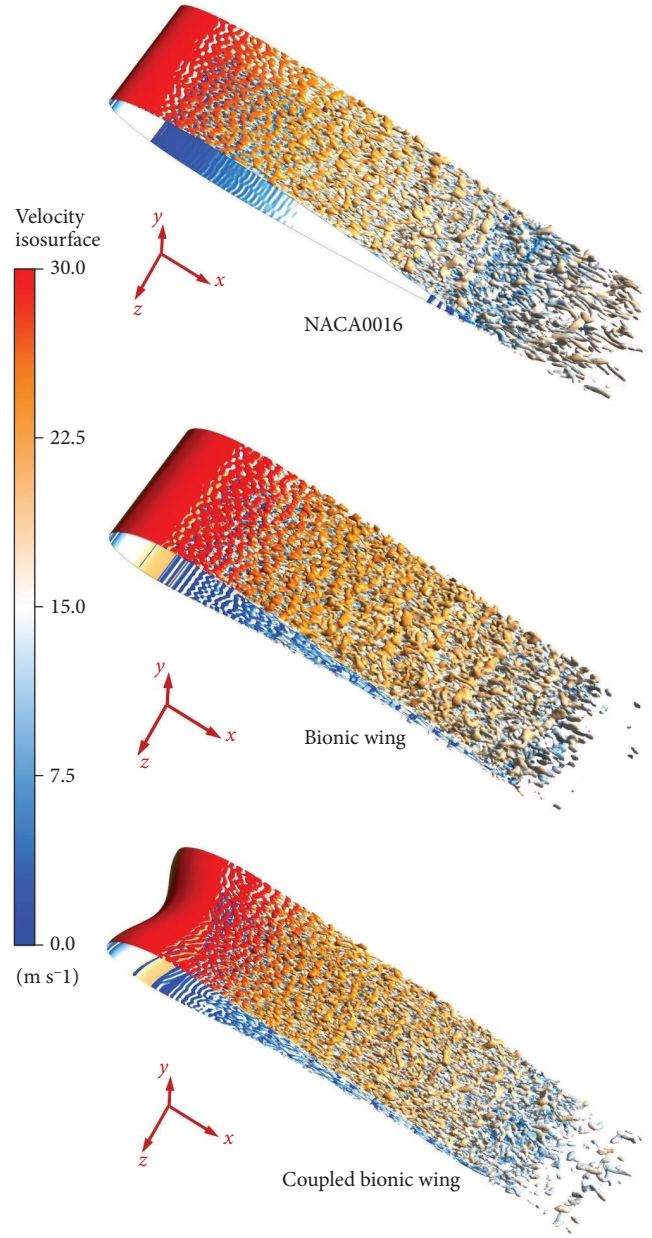

Figure 13: Isosurface of $Q = 5 \times 10^5$ colored by velocity magnitude at 0.5 s.

and lower surface. This means that the flow indeed becomes turbulent under strong adverse pressure gradient. Moreover, the unsmooth structures of coupled bionic wing causing the transition happened a little earlier, compared with that of bionic wing.

Using the vortex isosurface made by the Q-criterion, the level of vorticity and the scale of turbulence structure can be well-reflected, making it a good tool for instantaneous vortex visualization. The Q-criterion is defined as follows:

$$Q = \frac{1}{2}\left(\Omega_{ij}\Omega_{ij} - S_{ij}S_{ij}\right), \tag{18}$$

where Ω_{ij} and S_{ij} are the average tensor and average strain rate of the rotation speed, respectively. The isosurface of $Q = 5 \times 10^5\ s^{-2}$ colored by velocity magnitude are selected to further demonstrate the vortex's three-dimensional development in the vicinity of the studied wings, as shown in Figure 13. Since the angle of attack is 5°, the upper surface of the wing contains more details of turbulent vortex structure. It can be clearly seen that the attached laminar flow

starts to be disturbed where separation occurs on the upper surface of each wing. Due to the reduced spanwise coherence, the disturbed instability gradually develops into Tollmien–Schlichting waves, which will induce strong acoustic waves. Afterwards, with stretching and breaking along the flow direction, hairpin-like vortex structures emerge, develop, and break, the flow is therefore developed into fully turbulent, and broadband three-dimensional spatial acoustic waves will take the place. To be more specific, the vortex structure of NACA 0016 wing is prominent for its large scale, which is more obvious in the trailing edge and wake region of the wing. Note that at the lower surface, the flow is laminar, and the tube-like spanwise vortex can be observed at the trailing edge. After collision and mix with upper surface turbulence, the vortex become intensive and complicated. Comparatively, the vortex cores of two bioinspired wings are much smaller and broken, and present strong nonuniformity and discontinuity. Especially at lower surface, the flow is largely turbulent after transition at the front, which could favor the momentum exchange at the trailing edge. Thus, the vortex distribution is significantly reduced in terms of scale and scope. In particular, for the coupled bionic wing, the vortex structures are smaller and further divided due to the influence of the unsmooth structures compared to that of bionic wing. These factors will eventually influence the acoustic characteristics and will be discussed afterwards.

4.3. Acoustic Characteristics. The overall sound pressure level (OASPL) in the far-field is defined in the following equation:

$$\mathrm{OASPL} = 10\log_{10}\left(\frac{\sum_{i=1}^{n} p_i^2}{p_{\mathrm{ref}}^2}\right), \tag{19}$$

where p_i is the effective sound pressure at different frequency and $p_{\mathrm{ref}} = 2 \times 10^{-5}$ Pa is the reference acoustic pressure equal to the threshold of human hearing. We define 12 acoustic receivers, as illustrated in Figure 14, which are evenly distributed on the x–y plane circle at a distance of $10c$ from the leading edge of the wing with angular increment of 30°. In particular, the radiation angle of 0° corresponds to the direction of the free-stream, and the direction of 90° is located vertically above the wing. Since the distance between the wing and the acoustic receiver is more than twice the chord length, it can be considered as a geometric far field.

The far filed directivity distribution of OASPL of conventional NACA 0016 and two bioinspired wings are depicted in Figure 15. The angle of attack is set to AoA = 5° as greater noise-reduction effect exhibited under this condition. It can be seen that the OASPL of studied wings varies with the change of radiation angle. Each wing exhibits the "8-shaped" dipole feature with the sound source tends to radiate to upward and downward direction. The difference of shape does not lead to the change of directivity of the wing's SPL, which confirms the aforementioned theoretical analysis that the dipole source is predominant in the process of sound generation. Moreover, it is clearly demonstrated in the figure

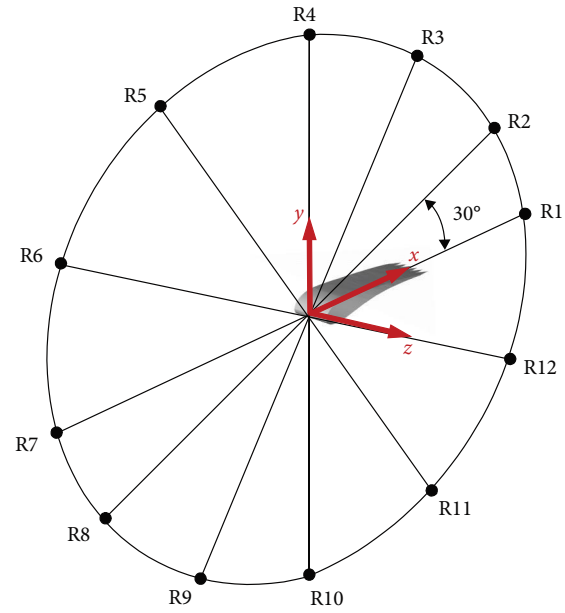

Figure 14: Acoustic receivers for SPL computation.

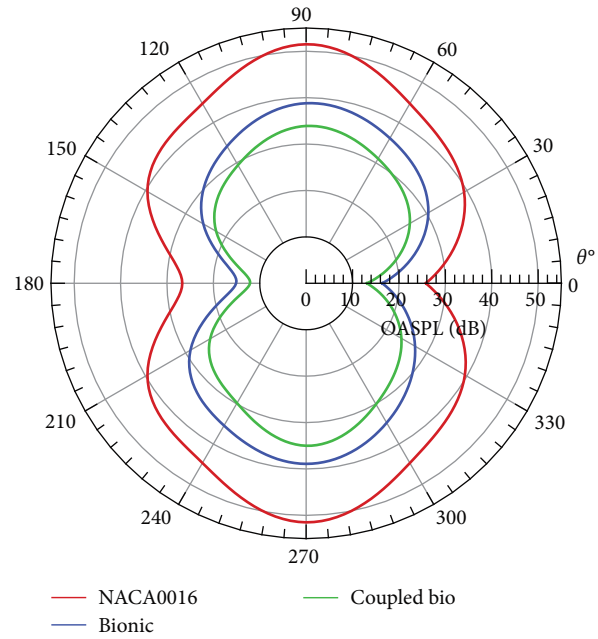

Figure 15: Directivity characteristics of OASPL.

that, at each acoustic receiver, the overall sound pressure level of the bioinspired wings has produced significant noise reduction effect. The numerical results show that the averaged overall SPL of the 12 acoustic receivers of the NACA 0016 airfoil, the bionic wing and the coupled bionic wing is 41.00, 30.12 and 25.85 dB, respectively.

The noise spectra indicate the variations of the SPL in different frequency ranges, which can illustrate the noise reduction effect in detail. The SPL can be calculated as follows:

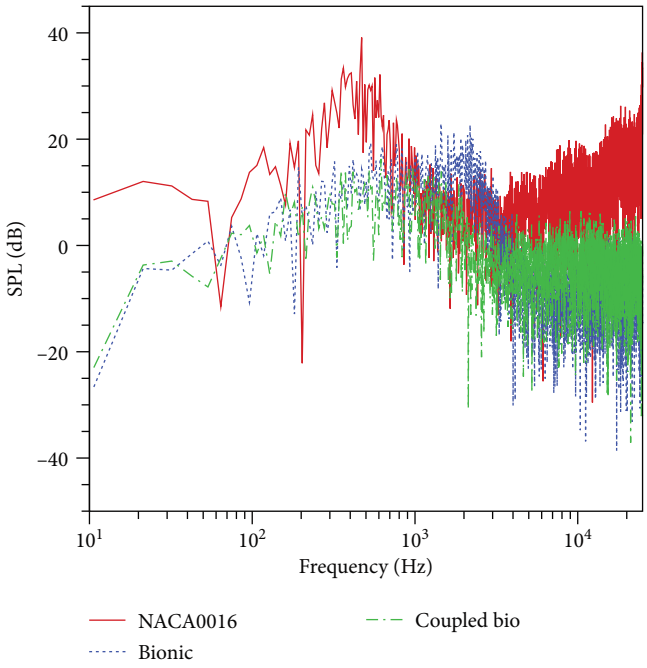

FIGURE 16: SPL spectra of the NACA 0016 and two bioinspired wings.

$$\mathrm{SPL} = 10\log_{10}\left(\frac{p^2}{p_{\mathrm{ref}}^2}\right), \tag{20}$$

where variables denote the same with previous OASPL definition. The SPL spectra by FFT at the acoustic receiver are computed considering all noise sources. Figure 16 shows the SPL spectra of the NACA 0016 and two other bioinspired wings at an azimuth angle of 90° (receiver R4), which generates mostly significant noise.

It can be seen from the spectrum characteristics that the noise of NACA 0016 airfoil has a distinct spectral peak, with the corresponding frequency of about 470 Hz and SPL of 39.12 dB, and the SPL in the high-frequency range is considerably high. Such obvious tonal characteristics is very likely caused by the trailing-edge laminar separation bubble. Comparatively, the noise spectra of the bioinspired wings are mainly broadband, without distinct tonal peak, and the SPL distributions over entire frequency range are basically lower than that of the NACA 0016. This leads to the consequence that bioinspired wings significantly reduce noise. Furthermore, although similar spectrum distributions are presented for two bioinspired wings, clear differences exist around frequency 3,000 Hz. The coupled bionic wing shows lower SPL below 3,000 Hz and slightly higher average value at above frequencies. This indicates that the unsmooth structures help shifting the low-frequency strong noise to high-frequency weak one, and further reducing the overall averaged SPL.

It is obvious that compared with NACA 0016 wing, two bioinspired wings both have significantly suppressed noise, with the average noise reductions of 10.88 and 15.15 dB, respectively. The coupled bionic wing with leading edge waves and trailing edge serrations performs better in noise control, offering an extra 4.27 dB average noise reduction. Combined with the directivity analysis of the total SPL, the application of bionic technology has remarkable advantages in controlling aeroacoustic noise. The following is a detailed analysis of the noise reduction mechanism.

4.4. Mechanism of Noise Reduction. As mentioned above, the owl-based wings have excellent noise-reduction characteristics, especially the wing with unsmooth structures. Unlike the conventional NACA series airfoil, the bioinspired airfoil based on barn owl wing has unique shape characteristics. This may result in the location and mechanism of noise generation different from that of conventional airfoils. Vortex sound theory holds that the coherent structures of vortex shedding play an important role in revealing the generation and dissipation mechanism of noise. The vortex attached to the wing surface changes the pressure fluctuation, and the process of vortex movement including stretching and breaking will produce aerodynamic noise. Generally, the root-mean-square (RMS) of the pressure to the time deviation $(\partial p/\partial t)_{RMS}$ can be used to characterize the intensity of the pressure fluctuation on wing surface, and the sound source can be determined. The definition is as follows:

$$\left(\frac{\partial p}{\partial t}\right)_{\mathrm{RMS}} = \sqrt{\frac{\sum_{i=1}^{n}(\partial p_i/\partial t)^2}{N}}, \tag{21}$$

where N is the number of samples; $\partial p_i/\partial t$ is the pressure change rate at the sampling point i, t is the time, and p_i is the pressure at the sampling point i. Figure 17 shows the distribution of each wing surface. It can be seen from the figure that for the NACA 0016 wing, the high-value distribution is mainly concentrated at two places. One is at the front of the upper wing surface, where coincides with flow transition region. The other place is at the trailing edge of the lower wing surface, where small laminar separation bubble exists. Consistent with the discussions in the previous chapter, the flow in the separation bubble is accompanied with unsteady vortex generation, movement, and detachment, in which laminar flow intensively join with upper stream and becomes turbulent. The transition causes the unevenness of local flow, and induces large pressure fluctuations. Therefore, these places are the main noise sources. However, for the two bioinspired wings, its special shape makes the lower surface flow transit to turbulent much earlier, thus produce a sound source at the front of lower surface. Moreover, the overall pressure fluctuation level around wing surface is considerably weakened. On this basis, the unsmooth structures of the coupled bionic wing further restrict the high-pressure fluctuation values to the "trough valley," with its intensity and distribution range decreased. This can be clearly observed from the front region of both the upper and lower surfaces, which means that the coupled bionic wing is superior in suppressing noise sources.

Meanwhile, the generation and propagation of sound source can be directly revealed from another perspective. The RMS of pressure fluctuations p' can well reflect the

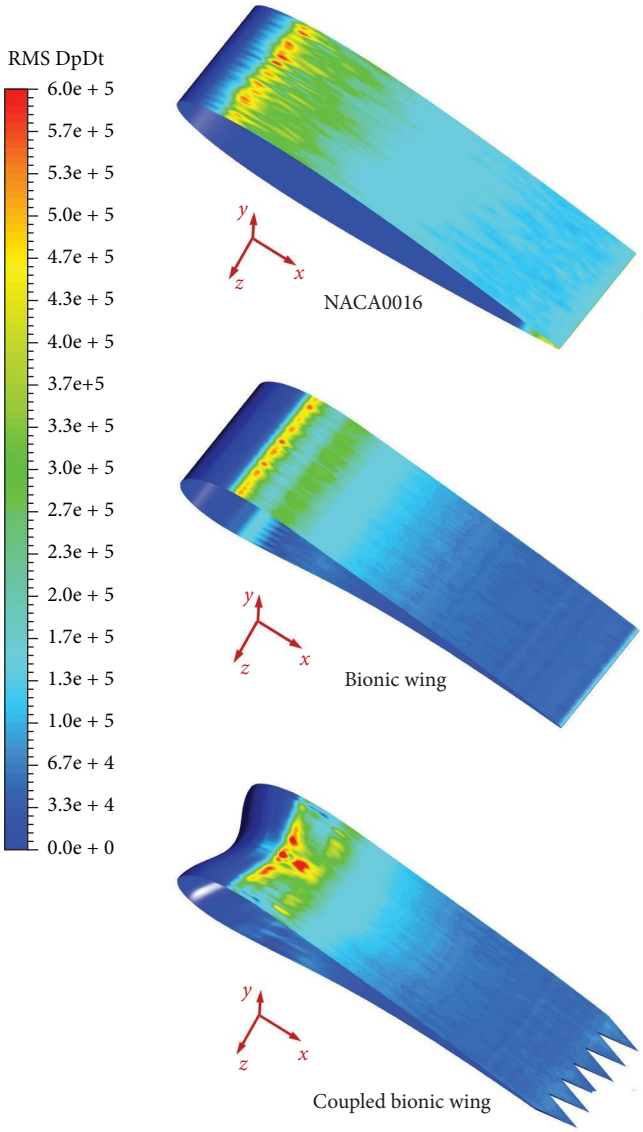

Figure 17: Comparison of contours of $\partial p/\partial t$ RMS.

distribution of turbulent noise in the flow field. The RMS of pressure fluctuation is defined as follows:

$$p'_{\mathrm{RMS}} = \sqrt{\frac{\sum_{i=1}^{n}(p - p_0)^2}{N}}, \tag{22}$$

where p is the instantaneous pressure, p_i is the time-average pressure, and the transient pressure fluctuation is defined as $p' = p - p_0$. Figure 18 shows the RMS distribution of pressure fluctuation at the vicinity of the wing maximum-span. It can be seen that compared with NACA 0016 wing, the RMS distribution of the two bioinspired wings is heavily reduced. Particularly, the large pressure fluctuation in the wake region has disappeared. This is largely due to the reason that two streams of fully developed turbulence meet at the trailing edge, rather than laminar separation bubble collide with

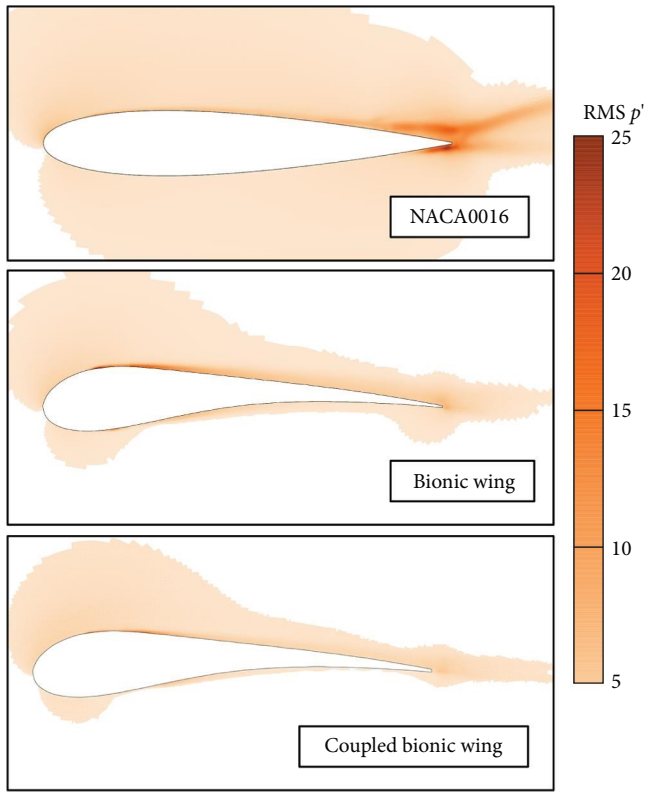

Figure 18: Comparison of contours of pressure fluctuations RMS.

upper turbulence as happened for NACA case. In fact, the reduction of pressure fluctuation releases the unsteady load of wing, which is crucial to the noise suppression of the bioinspired wings. For the two bioinspired wings, large pressure fluctuations mainly exist around the front upper surface, and the coupled bionic wing has lower values both at front and rear end, which is consistent with the RMS distribution of pressure to the time deviation as discussed earlier.

5. Conclusions

In this work, a LES coupled with FW–H numerical method is used to investigate the aerodynamic and aeroacoustic characteristics of two types of wings inspired by owl at low-Reynolds number condition. The flow field structures and noise reduction mechanism of bioinspired wings are further analyzed with the comparison of conventional NACA 0016 airfoil which has similar maximum relatively thickness of 16%c. The conclusions are as follows:

(1) The proposed two types of bioinspired wings, i.e., bionic wing and coupled bionic wing, both have excellent aerodynamic performances at low-Reynolds number condition. Comparison with NACA 0016 airfoil shows that much more lift is gained at a cost of small drag increment. And the unsmooth structures like leading edge waves and trailing edge serrations have little influence on aerodynamic characteristics at small working angles before stall.

(2) The acoustic results confirm that the dipole source still possesses the dominant role in sound field for the studied cases. The proposed two types of bioinspired wings demonstrate superior noise-reduction capabilities compared with NACA 0016 airfoil. The averaged noise level decreases 10.88 and 15.15 dB at 12 acoustic receivers for the bionic wing and the coupled bionic wing, respectively. This indicates that the owl-like airfoil is beneficial for suppressing noise, and the unsmooth structures has an additional noise-reduction effect. The spectral analysis further reveals that bioinspired spectral curves are much milder, without distinct tonal peak like that of NACA 0016 around low-frequency 470 Hz. Moreover, the unsmooth structures modifications further reduce the averaged SPL level of curve.

(3) The flow filed of the two bioinspired wing indicate that turbulence rather than laminar flow dominates the wing lower surface and no laminar separation bubble exists at the trailing edge. Compared with NACA 0016, bubble transition induced pressure fluctuation at the trailing edge of owl-based wing is significantly eliminated. Moreover, the unsmooth structures are advantageous for splitting the vortex into small scale, and restraining the noise generation. As a result, the coupled bionic wing exhibits a further suppression of pressure fluctuation. It is expected that the coupled bionic wing can be applied to designs of aeronautical machines to achieve better performance of noise reduction.

(4) For different flow conditions, the current bionic structural parameters, such as amplitude, wavelength, serration height, and width, might not be the optimal combination. Sensitivity analysis and parameter optimization are required for the enhancement of aerodynamic and aeroacoustic performances. Besides, recent research shows that the flow may have strong asymmetry and nonperiodicity when encountering uniformly distributed leading edge waves at high AoAs. It is speculated that the limitations of spanwise boundary conditions are likely to have a significant impact on the occurrence of this phenomena. This is a topic that is currently under investigation and the findings will be reported in the near future.

Nomenclature

Re: Reynolds number
c: Chord length
η: Normalized chordwise coordinate
ξ: Spanwise location
λ: Wavelength
A: Amplitude
h: Serration height
w: Serration width
AoA: Angle of attack
C_L: Lift coefficient
C_D: Drag coefficient
C_P: Pressure coefficient
C_f: Skin friction coefficient

Data Availability

The simulation data used to support the findings of this study are available from the corresponding author upon request.

Conflicts of Interest

The authors declare that they have no conflicts of interest.

Acknowledgments

The authors thank Wangbin Li for assistance in grid generation. The work was carried out at CFD center of AVIC Aerodynamic Research Institute, and the calculations were performed on supercomputer cluster "Jingqi-I".

References

[1] R. R. Graham, "The silent flight of owls," *The Aeronautical Journal*, vol. 38, no. 286, pp. 837–843, 1934.

[2] T. Liu, K. Kuykendoll, R. Rhew, and S. Jones, "Avian wing geometry and kinematics," *AIAA Journal*, vol. 44, no. 5, pp. 954–963, 2006.

[3] S. Klän, T. Bachmann, M. Klaas, H. Wagner, and W. Schröder, "Experimental analysis of the flow field over a novel owl based airfoil," *Experiments in Fluids*, vol. 46, pp. 975–989, 2009.

[4] S. Klän, M. Klaas, and W. Schröder, "The influence of leading edge serrations on the flow field of an artificial owl wing," in *28th AIAA Applied Aerodynamics Conference*, American Institute of Aeronautics and Astronautics, 2010.

[5] T. Geyer, E. Sarradj, and C. Fritzsche, "Silent owl flight: acoustic wind tunnel measurements on prepared wings," in *18th AIAA/CEAS Aeroacoustics Conference (33rd AIAA Aeroacoustics Conference)*, pp. 2230–2246, American Institute of Aeronautics and Astronautics, 2012.

[6] C. J. Ge, M. C. Ge, and P. Liang, "Investigation of noise mechanism based on owl wing," *Transactions of the Chinese Society for Agricultural Machineary*, vol. 44, pp. 292–296, 2013.

[7] W. Tian, Z. Yang, Q. Zhang et al., "Bionic design of wind turbine blade based on long-eared owl's airfoil," *Applied Bionics and Biomechanics*, vol. 2017, Article ID 8504638, 10 pages, 2017.

[8] G. Lilley, "A study of the silent flight of the owl," in *4th AIAA/CEAS Aeroacoustics Conference*, pp. 2340–2345, Confederation of European Aerospace Societies, 1998.

[9] M. S. Howe, "Aerodynamic noise of a serrated trailing edge," *Journal of Fluids and Structures*, vol. 5, no. 1, pp. 33–45, 1991.

[10] T. P. Chong, P. Joseph, A. Vathylakis, and M. Gruber, "On the noise and wake flow of an airfoil with broken and serrated trailing edges," in *17th AIAA/CEAS Aeroacoustics Conference (32nd AIAA Aeroacoustics Conference)*, pp. 2860–2878, American Institute of Aeronautics and Astronautics, 2011.

[11] T. P. Chong and P. F. Joseph, "An experimental study of airfoil instability tonal noise with trailing edge serrations," *Journal of Sound and Vibration*, vol. 332, no. 24, pp. 6335–6358, 2013.

[12] M. Gruber, P. Joseph, and T. Chong, "On the mechanisms of serrated airfoil trailing edge noise reduction," in *17th AIAA/CEAS aeroacoustics conference (32nd AIAA aeroacoustics conference)*, American Institute of Aeronautics and Astronautics, 2011.

[13] D. J. Moreau and C. J. Doolan, "The generation of tonal noise from sawtooth trailing-edge serrations at low Reynolds numbers," *The Aeronautical Journal*, vol. 120, no. 1228, pp. 971–983, 2016.

[14] H. Liu, Y. Lu, Y. Li, and X. Wang, "A bionic noise reduction strategy on the trailing edge of NACA0018 based on the central composite design method," *International Journal of Aeroacoustics*, vol. 20, no. 3-4, pp. 317–344, 2021.

[15] F. E. Fish and J. M. Battle, "Hydrodynamic design of the humpback whale flipper," *Journal of Morphology*, vol. 225, no. 1, pp. 51–60, 1995.

[16] Z. Wei, T. H. New, and Y. D. Cui, "An experimental study on flow separation control of hydrofoils with leading-edge tubercles at low Reynolds number," *Ocean Engineering*, vol. 108, pp. 336–349, 2015.

[17] B. Pena, E. Muk-Pavic, G. Thomas, and P. Fitzsimmons, "Numerical analysis of a leading edge tubercle hydrofoil in turbulent regime," *Journal of Fluid Mechanics*, vol. 878, pp. 292–305, 2019.

[18] K. Hansen, R. Kelso, and C. Doolan, "Reduction of flow induced tonal noise through leading edge tubercle modifications," in *16th AIAA/CEAS Aeroacoustics Conference*, American Institute of Aeronautics and Astronautics, 2010.

[19] T. P. Chong, A. Vathylakis, A. McEwen, F. Kemsley, C. Muhammad, and S. Siddiqi, "Aeroacoustic and aerodynamic performances of an aerofoil subjected to sinusoidal leading edges," in *21st AIAA/CEAS aeroacoustics conference*, American Institute of Aeronautics and Astronautics, 2015.

[20] S. Ito, "Aerodynamic influence of leading-edge serrations on an airfoil in a low reynolds number—a study of an owl wing with leading edge serrations," *Journal of Biomechanical Science and Engineering*, vol. 4, no. 1, pp. 117–123, 2009.

[21] S. Haeri, J. W. Kim, and P. Joseph, "On the mechanisms of noise reduction in aerofoil-turbulence interaction by using wavy leading edges," in *21st AIAA/CEAS Aeroacoustics Conference*, American Institute of Aeronautics and Astronautics, 2015.

[22] S. Narayanan, P. Chaitanya, S. Haeri, P. Joseph, J. W. Kim, and C. Polacsek, "Airfoil noise reductions through leading edge serrations," *Physics of Fluids*, vol. 27, no. 2, Article ID 025109, 2015.

[23] V. Clair, C. Polacsek, T. Le Garrec, G. Reboul, M. Gruber, and P. Joseph, "Experimental and numerical investigation of turbulence-airfoil noise reduction using wavy edges," *AIAA Journal*, vol. 51, no. 11, pp. 2695–2713, 2013.

[24] C. C. Paruchuri, S. Narayanan, P. Joseph, and J. W. Kim, "Leading edge serration geometries for significantly enhanced leading edge noise reductions," in *22nd AIAA/CEAS Aeroacoustics Conference*, vol. 30, American Institute of Aeronautics and Astronautics, 2016.

[25] L. Wang, X. Liu, and D. Li, "Noise reduction mechanism of airfoils with leading-edge serrations and surface ridges inspired by owl wings," *Physics of Fluids*, vol. 33, Article ID 015123, 2021.

[26] J. Bruce Ralphin Rose, S. Ganesh Natarajan, and V. T. Gopinathan, "Biomimetic flow control techniques for aerospace applications: a comprehensive review," *Reviews in Environmental Science and Bio/Technology*, vol. 20, pp. 645–677, 2021.

[27] V. T. Gopinathan and J. B. R. Rose, "Aerodynamic performance investigation of sweptback wings with bio-inspired leading-edge tubercles," *International Journal of Modern Physics C*, vol. 33, no. 3, Article ID 2250035, 2022.

[28] V. T. Gopinathan, J. Bruce Ralphin Rose, and M. Surya, "Investigation on the effect of leading edge tubercles of sweptback wing at low Reynolds number," *Mechanics & Industry*, vol. 21, no. 6, Article ID 621, 2020.

[29] V. T. Gopinathan and J. Bruce Ralphin Rose, "Aerodynamics with state-of-the-art bioinspired technology: tubercles of humpback whale," *Proceedings of the Institution of Mechanical Engineers, Part G: Journal of Aerospace Engineering*, vol. 235, no. 16, pp. 2359–2377, 2021.

[30] G. H. Liao, *Aerodynamic, acoustic characteristics of long-eared owl wing and its bionic application*, Ph.D. thesis, Jilin University, 2013.

[31] H. Johari, C. Henoch, D. Custodio, and A. Levshin, "Effects of leading-edge protuberances on airfoil performance," *AIAA Journal*, vol. 45, no. 11, pp. 2634–2642, 2007.

[32] X. M. Liu, J. Zhao, and D. Li, "Noise reduction mechanism of single-arc bionic blade with wave shape leading edge coupled with serrated trailing edge," *Journal of Xi'an Jiaotong University*, vol. 49, pp. 1–10, 2015.

[33] W. J. Chen, W. Y. Qiao, F. Tong, W. H. Duan, and T. J. Liu, "An experimental investigation of blade boundary layer instability noise with trailing edge serrations," *Acta Aeronautica Sinica*, vol. 37, no. 11, pp. 3317–3327, 2016.

[34] C. Rao, T. Ikeda, T. Nakata, and H. Liu, "Owl-inspired leading-edge serrations play a crucial role in aerodynamic force production and sound suppression," *Bioinspiration & Biomimetics*, vol. 12, no. 4, Article ID 046008, 2017.

[35] O. Marsden, C. Bogey, and C. Bailly, "Direct noise computation of the turbulent flow around a zero-incidence airfoil," *AIAA Journal*, vol. 46, no. 4, pp. 874–883, 2008.

[36] A. Bodling and A. Sharma, "Numerical investigation of low-noise airfoils inspired by the down coat of owls," *Bioinspiration & Biomimetics*, vol. 14, no. 1, Article ID 016013, 2018.

[37] F. Nicoud and F. Ducros, "Subgrid-scale stress modelling based on the square of the velocity gradient tensor," *Flow, Turbulence and Combustion*, vol. 62, no. 3, pp. 183–200, 1999.

[38] O. Lehmkuhl, I. Rodríguez, A. Baez, A. Oliva, and C. D. Pérez-Segarra, "On the large-eddy simulations for the flow around aerodynamic profiles using unstructured grids," *Computers & Fluids*, vol. 84, pp. 176–189, 2013.

[39] J. E. Ffowcs Williams and D. L. Hawkings, "Theory relating to the noise of rotating machinery," *Journal of Sound and Vibration*, vol. 10, no. 1, pp. 10–21, 1969.

[40] F. Farassat and K. S. Brentner, "The acoustic analogy and the prediction of the noise of rotating blades," *Theoretical and Computational Fluid Dynamics*, vol. 10, pp. 155–170, 1998.

[41] W. Chen, W. Qiao, F. Tong, L. Wang, and X. Wang, "Numerical Investigation of wavy leading edges on rod–airfoil interaction noise," *AIAA Journal*, vol. 56, no. 7, pp. 2553–2567, 2018.

[42] K. Jansen, "Large-eddy simulation of flow around a NACA, 4412 airfoil using unstructured grids," *Annual Research Briefs*, pp. 225–232, 1996.

[43] A. A. Oberai, F. Roknaldin, and T. J. R. Hughes, "Computation of trailing-edge noise due to turbulent flow over an airfoil," *AIAA Journal*, vol. 40, no. 11, pp. 2206–2216, 2002.

[44] C. Wagner, T. Hüttl, and P. Sagaut, *Large-eddy Simulation for Acoustics*, Vol. 20, Cambridge University Press, 2007.
[45] K. Karthik, M. Vishnu, S. Vengadesan, and S. K. Bhattacharyya, "Optimization of bluff bodies for aerodynamic drag and sound reduction using CFD analysis," *Journal of Wind Engineering and Industrial Aerodynamics*, vol. 174, pp. 133–140, 2018.
[46] W. F. King and E. Pfizenmaier, "An experimental study of sound generated by flows around cylinders of different cross-section," *Journal of Sound and Vibration*, vol. 328, no. 3, pp. 318–337, 2009.
[47] T. F. Brooks, D. S. Pope, and M. A. Marcolini, "Airfoil self-noise and prediction," (No. L-16528), 1989.
[48] M. Jafari, A. Sojoudi, and P. Hafezisefat, "Numerical study of aeroacoustic sound on performance of bladeless fan," *Chinese Journal of Mechanical Engineering*, vol. 30, no. 2, pp. 483–494, 2017.
[49] C. R. Marks, M. P. Rumpfkeil, and G. W. Reich, "Predictions of the effect of wing camber and thickness on airfoil self-noise," in *20th AIAA/CEAS Aeroacoustics Conference*, American Institute of Aeronautics and Astronautics, 2014.
[50] D. Ma, Y. Zhao, Y. Qiao, and G. Li, "Effects of relative thickness on aerodynamic characteristics of airfoil at a low Reynolds number," *Chinese Journal of Aeronautics*, vol. 28, no. 4, pp. 1003–1015, 2015.
[51] T. Nakano, N. Fujisawa, and S. Lee, "Measurement of tonal-noise characteristics and periodic flow structure around NACA0018 airfoil," *Experiments in Fluids*, vol. 40, pp. 482–490, 2006.